

RHEINISCHE FRIEDRICH-WILHELMUS-UNIVERSITÄT BONN

ADVANCED LABORATORY COURSE

PERFORMED ON: APRIL 4TH - 5TH, 2022

SUBMITTED ON: MAY 3, 2022

---

**A249: Laser Gyroscope**

---

*Authors*

Keito Watanabe  
Paarth Thakkar

*Tutor(s)*

Thorsten Groh  
Marc Vöhringer

**Abstract**

# Contents

<b>1</b>	<b>Introduction</b>	<b>2</b>
<b>2</b>	<b>Theory</b>	<b>4</b>
2.1	Gyroscopes . . . . .	4
2.1.1	The Sagnac Effect . . . . .	4
2.1.2	Ring Laser Gyroscopes . . . . .	5
2.2	Optical Cavities . . . . .	6
2.2.1	Cavity Modes . . . . .	6
2.2.2	Finesse . . . . .	7
2.2.3	Cavity-Ring-Down Technique . . . . .	7
2.2.4	Pound-Drever-Hall Locking . . . . .	7
2.2.5	Lock-In Effect . . . . .	8
2.3	Allan Deviation . . . . .	8
<b>3</b>	<b>Pre-Lab Exercises</b>	<b>9</b>
3.1	Task 1: Getting Started . . . . .	9
3.2	Task 2: Allan Deviation . . . . .	11
3.3	Task 3: Rotation Rate of Earth . . . . .	14
<b>4</b>	<b>Experimental Set-Up and Procedure</b>	<b>17</b>
4.1	Experimental Set-Up . . . . .	17
4.2	Procedure . . . . .	17
4.2.1	Free Spectral Range . . . . .	17
4.2.2	PDH Error Signal and PID Optimization . . . . .	18
4.2.3	Cavity Ring-Down . . . . .	19
4.2.4	Scale Factor . . . . .	19
4.2.5	Allan Deviation . . . . .	21
<b>5</b>	<b>Results and Discussion</b>	<b>22</b>
5.1	Free Spectral Range . . . . .	22
5.2	PDH Error Signal . . . . .	23
5.3	Cavity Ring-down . . . . .	23
5.4	Scale Factor . . . . .	23
5.5	Allan Deviation . . . . .	23
5.6	Rotation Rate of the Earth . . . . .	24
<b>6</b>	<b>Conclusion and Outlook</b>	<b>25</b>
<b>7</b>	<b>Acknowledgements</b>	<b>26</b>
<b>8</b>	<b>Appendix</b>	<b>28</b>

# Chapter 1

## Introduction

The rotation of the Earth has been investigated ever since the advent of calenders. The first measurements for the rotation of the Earth has been done by observing the apparent position of a fixed star, allowing the Mayans to obtain measurements with relative uncertainties of around  $10^{-5}$  [1].

Today, the rotation of the Earth is measured using interferometry, where radio telescopes all around the world are linked to construct a very-long base-interferometer system (VLBI). Fig. 1.0.1 show the locations of all radio telescopes under the CONT17 campaign, a continuous VLBI session held for two weeks in 2017 [2]. The relative uncertainties that are obtained reach approximately  $10^{-10}$ . Today, the rotation of the Earth is measured to be approximately  $72.92 \text{ prad s}^{-1}$  along its rotation axis [1].

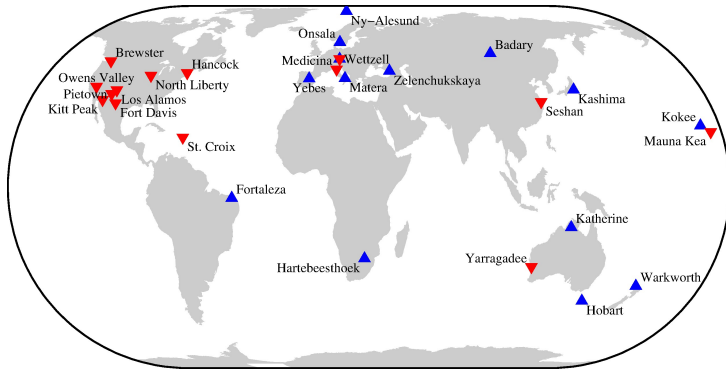


Figure 1.0.1: Radio telescopes used for CONT17. Both blue and red markers indicate legacy stations used for measurements in past sessions.

Determining the rotation of the Earth allows us to understand the vast phenomena that occur on Earth, including tidal breaking, seasonal variations, and the Chandler wobble, the nutation that occurs with Earth's rotation axis. Furthermore, climate change has a strong effect on the rotation rate as the melted ice from the polar ice caps gravitate towards the equator, increasing the angular momentum and thus the rotation period of Earth. This is shown to increase at a rate of  $1.2 \mu\text{s}$  per year [1].

While the VLBI can determine the rotation rate with high precision, due to the operation times the temporal resolution is low. As such, transient events such as earthquakes and tides cannot be resolved. As of such, laser gyroscopes have been employed to resolve such details. While it lacks in the long-term stability of VLBI, they have a temporal resolution of approximately an hour or less [3]. The G-ring at the German Fundamentalstation Wettzell is one of the best ring laser gyroscopes with a sensitivity of around  $12 \text{ prad/s}/\sqrt{\text{Hz}}$  [1]. See Fig. 1.0.2 for an image and the setup of the G-Ring gyroscope. Ring laser gyroscopes are still explored today to describe other phenomena from the Earth's rotation such as the Lense-Thirring Effect, and gyroscopes such as the GINGERino have been proposed to measured such quantities [4].

In our experiment, we use a ring laser gyroscope to attempt to measure the rotation rate of the Earth. This is done by employing the Sagnac effect, which allows us to determine the rotation of an inertial system by the path length difference between two light beams. To observe the quality of the constructed laser gyroscope, we measure optical cavity parameters such as the free spectral range, PDH locking error signals, lock-in threshold, and the finesse. We further quantify the stability and sensitivity

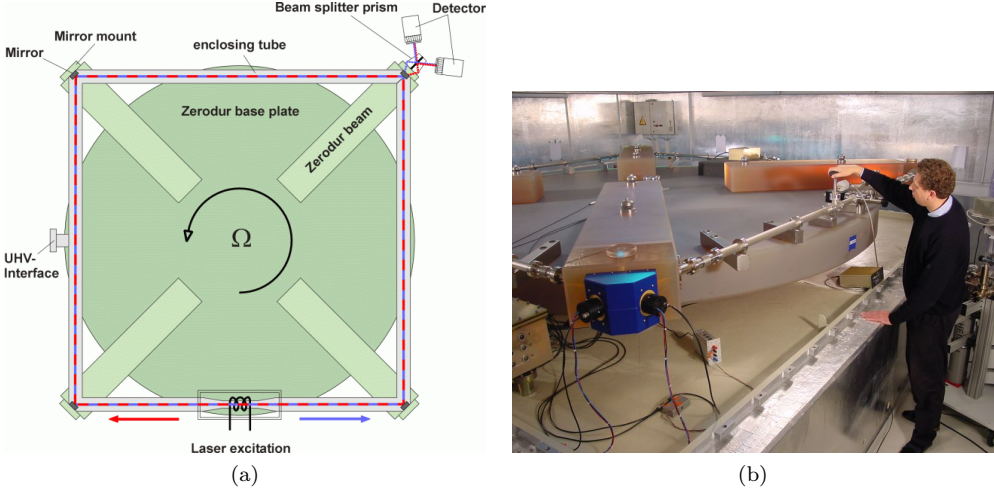


Figure 1.0.2: The G-Ring gyroscope at the Fundamentalstation Wettzell. (a): The setup of the gyroscope. (b): Image of the G-ring. Obtained from Ref. [3].

of the gyroscope by determining the Allan deviation.

This paper is structured as follows. Chapter 1 motivates the experiment by elaborating on the usage of ring laser gyroscopes to determine the rotation rate of the Earth. Chapter 2 describes the theory behind the quantities measured in the experiment. Chapter 3 describes the setup used in our experiment and the method used to determine the relevant quantities for each part of our experiment. Chapter 4 shows the pre-laboratory tasks that were required before starting the experiment. Chapter 5 shows the results that we have obtained and discussions related to the results. Finally, we summarize our findings and address possible outlooks for our experiment in Chapter 6.

# Chapter 2

## Theory

### 2.1 Gyroscopes

#### 2.1.1 The Sagnac Effect

The Sagnac effect tells us that whilst the motion between two inertial frames cannot be distinguished, two rotating frames can be distinguished, allowing one to directly measure the rotation rate of an inertial system [1]. This effect was first observed by George Sagnac in 1913, whom believed that this experiment was a proof that aether exists in an inertial frame [5]. This, however, was disproven by Max von Laue in 1911 where he showed that the Sagnac effect was compatible with special relativity [6]. However, the interpretation of the Sagnac effect due to the general theory of relativity is still investigated today, even though it is already well-known in literature [7]. In our analysis, we utilize the Sagnac effect on a gyroscope to measure the rotation rate of the Earth.

To observe the Sagnac effect, we consider an interferometer setup with light propagating with wavelength  $\lambda$  enclosing an area  $\vec{A}$  with perimeter  $P$ . Placing such a setup onto a rotating platform with frequency  $\vec{\Omega}$ , we observe that the optical path that each light travels changes. For example, if the table rotates counter-clockwise, then the path of the co-rotating light increases, while that of the other light decreases (see Fig. 2.1.1). The Sagnac effect then tells us the resulting phase shift between the two lights:

$$\delta\phi = \frac{8\pi\vec{A} \cdot \vec{\Omega}}{c\lambda} \propto \vec{A} \cdot \vec{\Omega}. \quad (2.1.1)$$

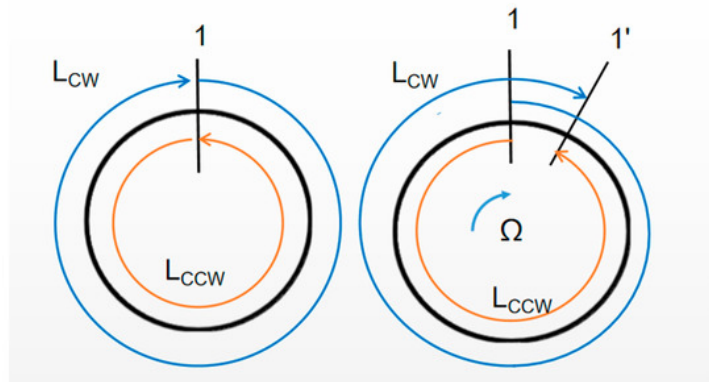


Figure 2.1.1: The Sagnac effect. *Left:* Setup without rotation. The beam moving clockwise (blue) and counter-clockwise (orange) have the same optical path length. *Right:* Setup with a clockwise rotation  $\Omega$ . The path length of the clockwise beam is larger than that of the counter-clockwise beam. Obtained from Ref. [8].

A more detailed derivation using the relativistic law of velocity addition can be found in Ref. [7].

## 2.1.2 Ring Laser Gyroscopes

### Active Ring Laser Gyroscopes

In order to incorporate the Sagnac effect within our experiment, we utilize ring laser gyroscopes. A laser is placed within an enclosed cavity, and emits two counter-propagating beams. Such beams reflect off mirrors and interfere at the end of their propagation. When rotating the platform in which such setup is placed, different interference patterns can be observed, and transforms the ring cavity system into a cavity resonator. The corresponding beat frequency  $\delta\nu$  observed is then the Sagnac frequency, which is given as such:

$$\delta\nu = \frac{4\vec{A} \cdot \vec{\Omega}}{P\lambda}. \quad (2.1.2)$$

In our experiment, we only consider square ring cavities so that  $A = L^2$  and  $P = 4L$ , where  $L$  is the path length of each arm. As such, we can simplify Eq. 2.1.2 as such:

$$\delta\nu = \frac{L\Omega}{\lambda} = n\Omega, \quad (2.1.3)$$

where  $n = L/\lambda$  is the number of nodes of the light field in each arm. Thus the Sagnac frequency is proportional to the rotation rate of the inertial system [1].

### Passive Ring Laser Gyroscopes

In contrast to the active ring laser gyroscope, in which the laser is contained within the ring cavity, the passive ring laser gyroscope places the laser source outside of the cavity system. In this system, the external laser is locked to the counter-propagating modes of the resonator. By placing the laser outside of the resonator, we can reduce the systematic effects due to the lasing medium and the lock-in effect (see Sec. 2.2.5), and also increase the available light power for the beam. This method, however, also introduces an added complexity of laser locking [1]. See Fig. 2.1.2 for a comparison between the two systems. In our experiment, we use the passive ring laser gyroscope and thus laser locking becomes an importance in our measurements.

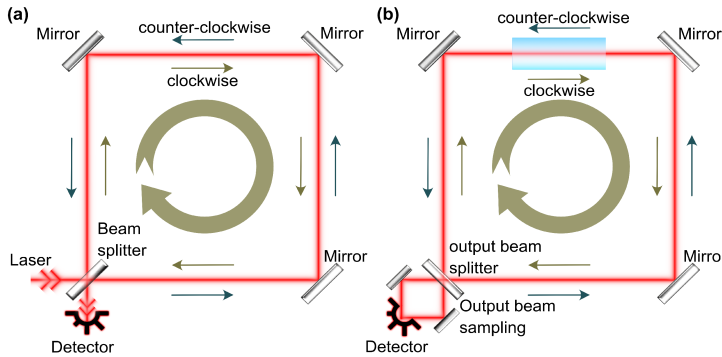


Figure 2.1.2: Ring laser gyroscope systems. *Left:* Passive, *Right:* Active. Obtained from Ref. [9].

### Gyroscope Sensitivity

The sensitivity of the ring laser gyroscope depends on a variety of factors, namely the wavelength  $\lambda$ , arm length  $L$ , finesse  $F$  of the resonator (see Sec. 2.2.2), and the shot-noise limited detection given by the number of photons  $N = P_{\text{opt}}/h\nu = P_{\text{opt}}\lambda/hc$  detected per unit time.  $P_{\text{opt}}$  represents the optical power given to the laser. Combining all such factors, we obtain the sensitivity of the ring laser gyroscope for an integration time  $\tau$  as such:

$$\delta\Omega = \frac{1}{4} \frac{c}{L^2 F} \sqrt{\frac{ch\lambda}{P_{\text{opt}}}} \frac{1}{\sqrt{\tau}}. \quad (2.1.4)$$

This gyroscope sensitivity can be directly compared with the Allan deviation  $\sigma_{\text{ad}}$  that determines the instability of a measurement for some averaged integration time  $\tau$  (see Sec. 2.3).

## 2.2 Optical Cavities

A cavity is a hollow conductor which contains electromagnetic waves going in and reflecting off the walls. At certain frequencies, these reflected waves form standing waves which correspond to the resonant modes of the cavity. An optical cavity consists of an arrangement of mirrors, which produces standing electromagnetic waves. In our setup, instead of the traditional Fabry-Pérot interferometer, which consists of two opposing flat mirrors, we use four mirrors. Nevertheless, the same principles of resonance modes applies.

### 2.2.1 Cavity Modes

The solution to optical resonators with parabolic mirrors and homogeneous medium is given by the Hermite-Gaussian modes. The Hermite-Gaussian modes are the solution to the paraxial Helmholtz equation, when considering Cartesian coordinates with the beam propagating along the  $z$ -axis (Fig. 2.2.1).

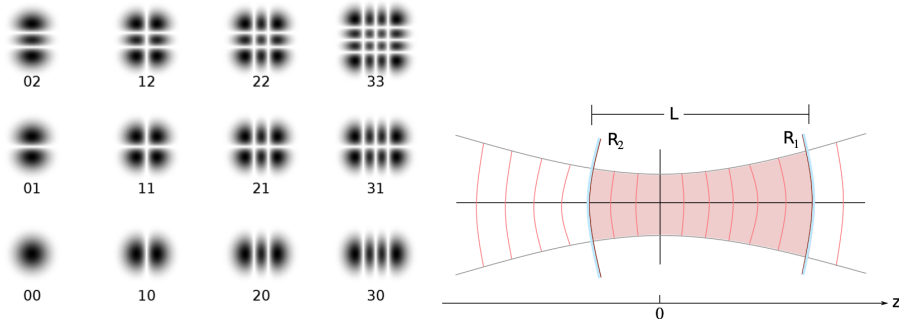


Figure 2.2.1: Hermite-Gaussian Transverse Electromagnetic Mode (TEM <sub>$l,m$</sub> ) (left) and the beam's wave-front between two mirrors of radii  $R_1$  and  $R_2$  with a separation of length  $L$ , inside a cavity [1].

The Hermite-Gaussian modes are also called Transverse Electromagnetic Mode (TEM) and are labelled as TEM <sub>$m,n$</sub> , where  $m, n \in \mathbb{N}^{\geq 0}$  are the integers, which represent the order of Hermite-polynomials along the  $x$  and  $y$  direction. The resonance frequency is given by

$$\nu_{l,m,n} = \delta\nu_{\text{FSR}} \left( l + (m + n + 1) \frac{\delta\zeta}{\pi} \right), \quad (2.2.1)$$

where  $l \in \mathbb{N}^{\geq 0}$  represents the different longitudinal nodes. The spacing between these longitudinal modes is given by the free spectral range,  $\delta\nu_{\text{FSR}}$ ,

$$\delta\nu_{\text{FSR}} = \frac{c}{P}. \quad (2.2.2)$$

The fundamental mode, TEM<sub>0,0</sub> is the Gaussian mode and is used for locking the lasers beam in our setup, as can be seen in Fig. 4.2.4. In order to achieve stability, the following condition on the radii of two mirrors,  $R_1$  and  $R_2$ , has to be met

$$0 \leq g_1 g_2 = \left( 1 + \frac{L}{R_1} \right) \left( 1 + \frac{L}{R_2} \right) \leq 1. \quad (2.2.3)$$

The above condition is true for a two mirror setup. In order to extend this to four mirror setup, we simply compute the magnitude of eigenvalues of ABCD transfer matrix for the roundtrip.

### Airy Lineshape and Optical Cavity Ringing

We expect the power transmitted through the cavity to have a Lorentzian like lineshape, called an Airy function, when the laser is scans through the frequencies of coupled modes. This occurs even with cavities with high Finesse cavities because the laser sweeps through different frequencies faster than the storage time of the cavity. This does not allow the cavity to recover and fill itself when resonance is approached. This leads to a beat, as the evolving field inside and the incoming field start to interfere and create an oscillatory behaviour.

### 2.2.2 Finesse

The Finesse of a cavity essentially quantifies the number of bounces a beam makes before leaking out or being absorbed. Mathematically, it is the ratio of the free spectral range,  $\delta\nu_{\text{FSR}}$ , to the spectral linewidth  $\delta\nu_{1/2}$ , the Full Width Half Maximum (FWHM) of the transmission peak. Since it is inversely proportional to the FWHM, a high finesse equals a narrow resonance line and vice versa. A narrow resonance line is better for high precision frequency applications. The formula is given by

$$\mathcal{F} = \frac{\delta\nu_{\text{FSR}}}{\delta\nu_{1/2}} \approx \frac{\pi\sqrt{\mathcal{R}}}{1 - \mathcal{R}}, \quad (2.2.4)$$

where  $\mathcal{R} = \sqrt{\mathcal{R}_1\mathcal{R}_2\mathcal{R}_3\mathcal{R}_4}$ , where  $\mathcal{R}_i$  is the reflectivity of the cavity mirrors.

### 2.2.3 Cavity-Ring-Down Technique

To precisely compute the finesse of mirrors in the cavity, we employ ring-down technique. In this, we look at how the power in the cavity evolves temporally, when the cavity-locked laser is switched off quickly. In order to achieve the latter, we switch the RF signal driving the Acousto-Optical Modulator (AOM).

Neglecting the losses in the cavity medium, the time evolution of the laser intensity is given by

$$I(t) = I_0 \mathcal{R}^{2t/\tau_r} = I_0 \exp\left(-\frac{t}{\tau_{dec}}\right), \quad (2.2.5)$$

where  $\tau_r = P/c$  is the roundtrip time and  $\tau_{dec}$  is the decay time, which is given by

$$\tau_{dec} = -\frac{\tau_r}{\log \mathcal{R}^2} = -\frac{P}{c \log \mathcal{R}^2}. \quad (2.2.6)$$

### 2.2.4 Pound-Drever-Hall Locking

Pound-Drever-Hall (PDH) technique is a way to stabilize the frequency of light emitted by the laser by locking to a stable cavity. The central idea of this technique is the following - phase modulated light, typically by an Electro-Optical Modulator (EOM), consisting of carrier frequency  $\omega$  and two side bands  $\Omega$  is inserted into the cavity. The reflected light from the cavity is recorded with a fast photodiode, which consists of the two unaltered side bands and a phase shifted carrier. This phase shifted carrier is mixed with the local oscillator and passed through a low pass filter in order to remove high frequency components. The resulting signal shows how far off the laser carrier is from resonance. This signal is then fed into the Proportional-Integral-Derivative (PID) controller, which then applies an error signal (Fig. 2.2.2) and which is then fed back into the cavity, allowing the laser to remain locked.

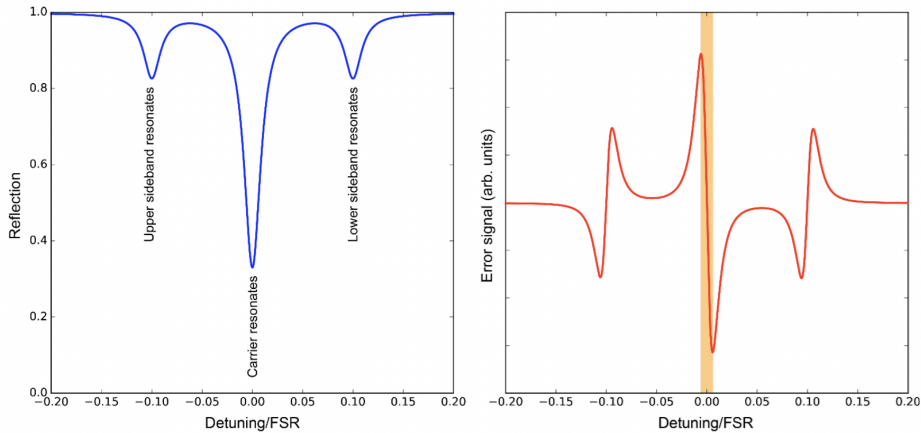


Figure 2.2.2: Pound-Drever-Hall (PDH) cavity reflection (left), which shows the ingoing carrier frequency along with two sidebands. The error signal after frequency demodulation (right) that is used for PID feedback to stabilize the laser [10].

To the first order, the frequency components can be approximated to:

$$E_{\text{in}} = E_0 e^{i(\omega t + \beta \sin(\Omega t))} \approx E_0 \left( J_0(\beta) e^{i\omega t} + J_1(\beta) e^{i(\omega + \Omega)t} - J_1(\beta) e^{i(\omega - \Omega)t} \right), \quad (2.2.7)$$

where  $J_k$  are the Bessel functions and  $\beta$  is the modulation depth. The reflection coefficient is given by  $F(\omega) = E_{\text{ref}}/E_{\text{in}}$ .

The slope of the error signal is given by

$$\epsilon \propto -\frac{4}{\pi} \sqrt{P_c P_s} \delta\nu_{1/2}, \quad (2.2.8)$$

where  $P_c$  is the carrier power given by  $P_c = J_0^2(\beta) |E_0^2|$  and  $P_s$  is the sideband power which is given by  $P_s = J_1^2(\beta) |E_0^2|$ . Selecting good PID parameters for correcting both fast and slow laser lock disturbances can help achieve frequency stabilization to a fraction of the cavity linewidth.

### 2.2.5 Lock-In Effect

The lock-in effect occurs when the two oscillator modes with a small delta frequency between them start oscillating at the same frequency due to weak coupling between them. This is a common occurrence in the field of physics and the best example are two oscillating pendulums hung upon the same wooden wall, oscillating with slightly different frequency eventually synchronize and start oscillating at the same frequency. In general, the frequency difference between two pendulums is,

$$\delta f = \sqrt{f_0^2 - f_L^2}, \quad (2.2.9)$$

where  $f_L$  is the lock-in threshold below which the two pendulums synchronize. This effect can also be seen in RF electronics and optics.

In our setup, we can encounter this phenomenon due to the back scattering losses in the mirrors of the cavity, which is usually only a few ppm, but can amplified due to presence of dust. These losses lead to a delta in the frequency, which leads to the lock-in effect. The lock-in threshold is given by

$$\Omega_L = \frac{c\lambda^2 r_s}{32\pi A d}, \quad (2.2.10)$$

where  $\lambda$  is the laser wavelength,  $A$  is the enclosed area of the cavity,  $d$  is the cavity mode beam diameter and  $r_s$  the fraction of backscattering as compared to other losses [11].

With the present setup, the lock-in threshold is much greater than the Earth rotation, which will limit our ability to measure it accurately. In order to reduce the locking threshold, a larger ring and reduced scattering losses will be required.

## 2.3 Allan Deviation

The Allan deviation is used to quantify the instability of any device that measures differences in frequencies. Assuming that the measurement is only limited by the photon shot-noise (amongst others), we can describe the Allan variance as the deviation between temporal averages of measurements  $y$  over some time interval or integration time  $\tau$ :

$$\sigma_{\text{ad}}^2 = \frac{1}{2M} \sum_{n=1}^M (\bar{y}(\tau)_{n+1} - \bar{y}(\tau)_n)^2, \quad (2.3.1)$$

where  $M$  is the number of samples. The Allan deviation is then the square root of the variance.

The Allan deviation is especially helpful to understand the sensitivity in gyroscopes. Imposing the same assumptions as above, we can describe the Allan deviation with typical shot noise scaling  $\propto 1/\sqrt{\tau}$  as such:

$$\sigma_{\text{ad}} = \mathcal{A} \tau^m = \frac{\mathcal{A}}{\sqrt{\tau}}, \quad (2.3.2)$$

where  $\mathcal{A}$  (given in rad/s/ $\sqrt{\text{Hz}}$ ) is known as the shot-noise limited sensitivity of the gyroscope and  $m = -\frac{1}{2}$ . This value can be directly compared with the theoretical gyroscope sensitivity (per integration time) described in Eq. 2.1.4 [1].

# Chapter 3

## Pre-Lab Exercises

Before conducting the experiment, we were required to determine the rotation rate of the Earth using our phone. Our phones contain a microelectromechanical system (MEMS), which is a portable and inexpensive inertial sensor that track the motion of the phone. Using the application **phyphox** constructed by RWTH Aachen University, we evaluated the capabilities of the MEMS gyroscope within our phones.

### 3.1 Task 1: Getting Started

We downloaded the **phyphox** app made by RWTH Aachen University, and we played around with the Gyroscope function. We rotated the phone in several directions to observe the relationship between the orientation of the phone and the corresponding coordinates used in the application. This is shown in Fig. 3.1.1. Fig. 3.1.2 - 3.1.4 show the corresponding time series for the  $x, y, z$  coordinates for each rotation that we performed.

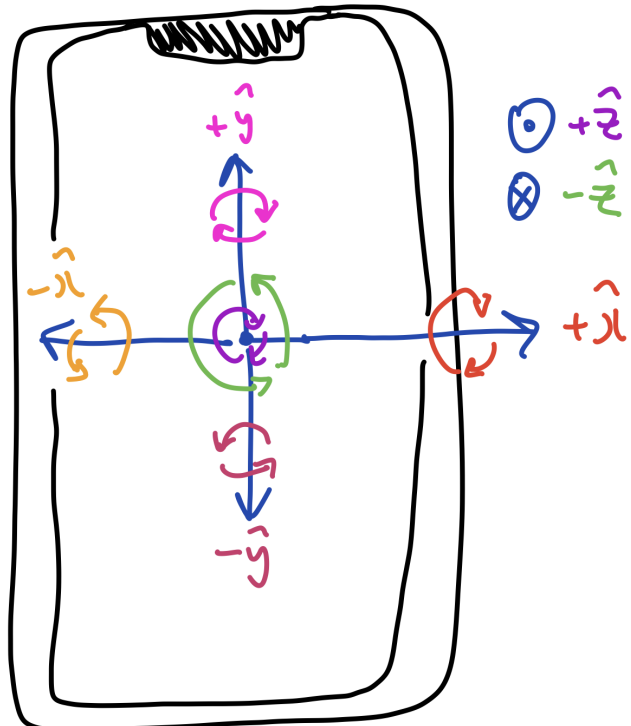
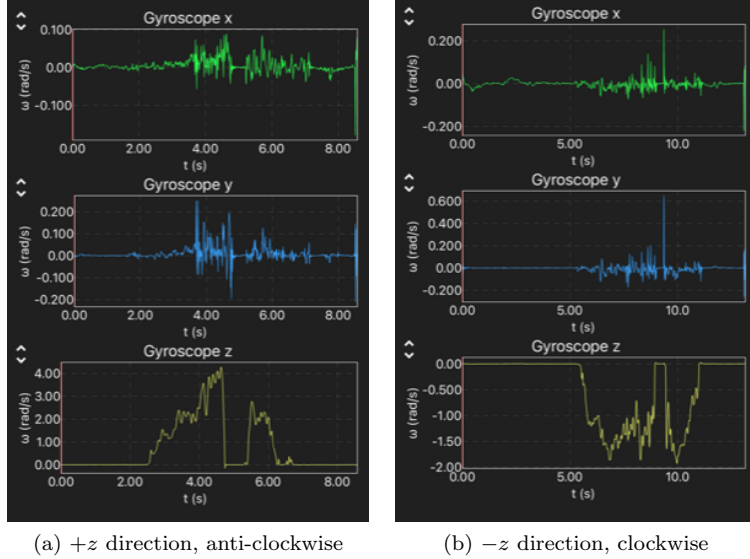


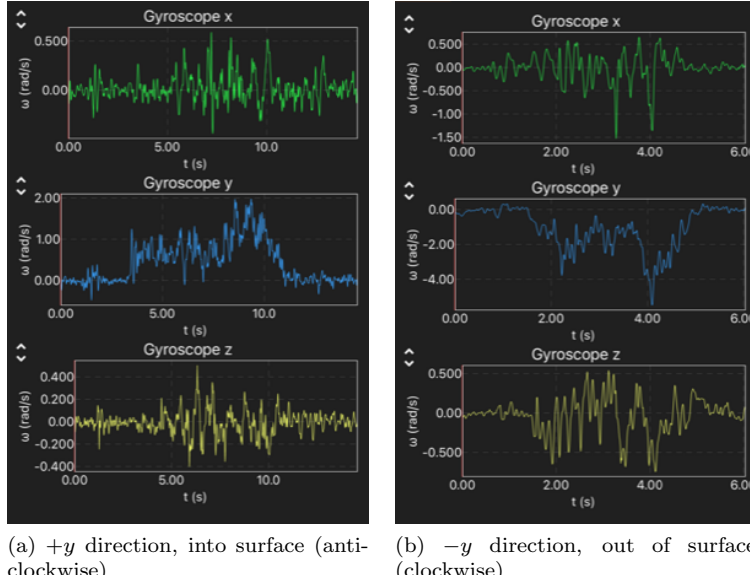
Figure 3.1.1: Sketch of the phone used to measure the gyroscope with its relevant  $x, y, z$  coordinates and sense of rotation. The sense of rotation is color coded with each rotation axis, and the direction of the axis is indicated by the blue arrows.



(a)  $+z$  direction, anti-clockwise

(b)  $-z$  direction, clockwise

Figure 3.1.2: The time series of the  $x, y, z$  coordinates shown from the `phyphox` application when the phone was rotated parallel to the surface. This corresponds to rotations in the  $z$ -direction. Note the large amplitudes in the time series, which indicates rotations in the relevant axis.



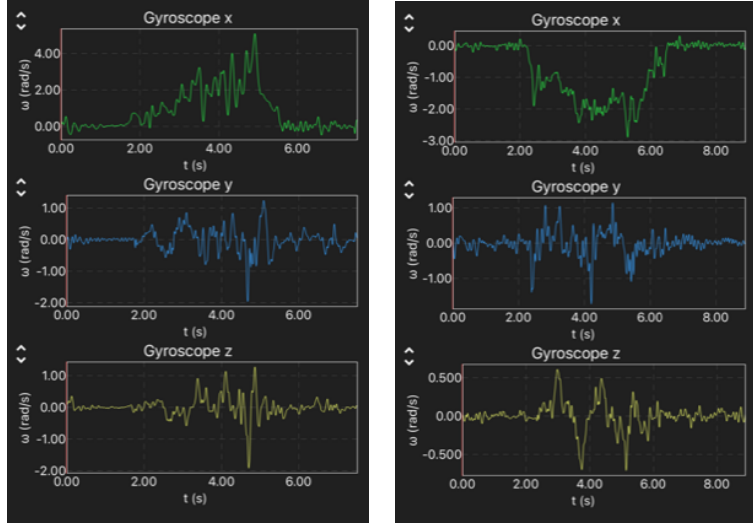
(a)  $+y$  direction, into surface (anti-clockwise)

(b)  $-y$  direction, out of surface (clockwise)

Figure 3.1.3: Same as Fig. 3.1.2 but for rotations into / out of the surface, corresponding to rotations in  $y$ -direction.

To save the rotation rates and import it into the computer for further analysis, the **Export Data** feature can be utilized. This will save the data as a `.zip` file that contains the raw data, the software and specifics regarding the device used, and the system time in which the experiment was started and finished. All such files are saved as `.csv` formats. An example for the raw data is shown in the Appendix section.

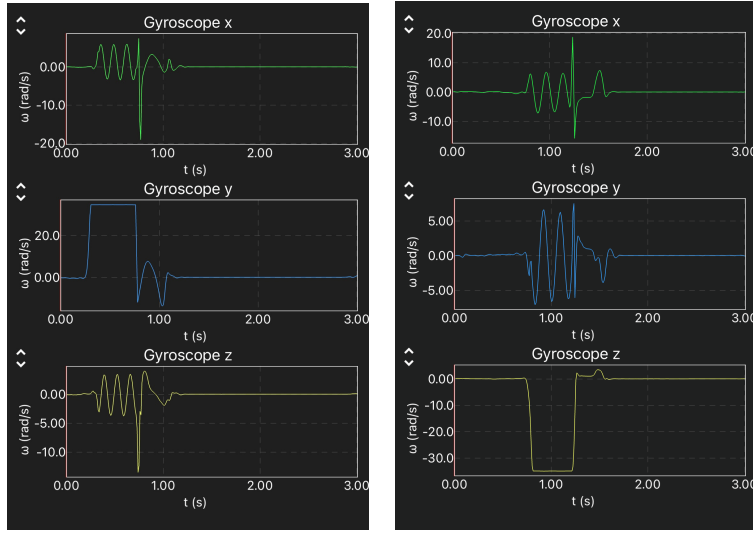
To obtain a faster rotation rate, we applied maximal torque on each end of the phone such that the rotation at each axis was maximal. This was done at an adequate height to ensure the rotation rate was properly measured. Several cushions were placed on top of a bed to ensure that the phone does not break. Fig. 3.1.5 show the time series of the  $x, y, z$  coordinates in the  $+y$  and  $-z$  directions. Performing the measurement in such a way yields a more notable and stable measurement of the rotation rate



(a)  $+x$  direction, rotation towards user (anti-clockwise)

(b)  $-x$  direction, rotation away from user (clockwise)

Figure 3.1.4: Same as Fig. 3.1.2 but for rotations towards / away the user, corresponding to rotations in  $x$ -direction.



(a)  $+y$  direction

(b)  $-z$  direction

Figure 3.1.5: Same as Fig. 3.1.2 but for fast rotations in the (a)  $+y$  and (b)  $-z$  direction.

## 3.2 Task 2: Allan Deviation

To determine the Allan deviation of the phone's MEMS gyroscope, we placed our phone on a platform with minimal disturbance and took the measurement for approximately one hour. Fig. 3.2.1 shows the time series for each gyroscopic component obtained. From the time series alone, we observe that there are no significant deviations in the measurements in each direction.

We then performed a Fast Fourier Transform (FFT) using the built-in package `scipy.fft` to obtain the plot in the frequency domain. Fig. 3.2.2 shows the Fourier spectrum in each gyroscopic component. We observe that up until around a frequency of 1.5 Hz, the frequency spectrum shows the noise of the measurement. After this point, we observe that the spectrum drops significantly, which indicates that the gyroscope readings occur after this point in the frequency domain. We observe that there is a dip in the spectrum at around 2.2 Hz as well as a small peak at approximately 18 Hz for the measurement in the x direction. This may be caused by the location in which the MEMS gyroscope is placed within

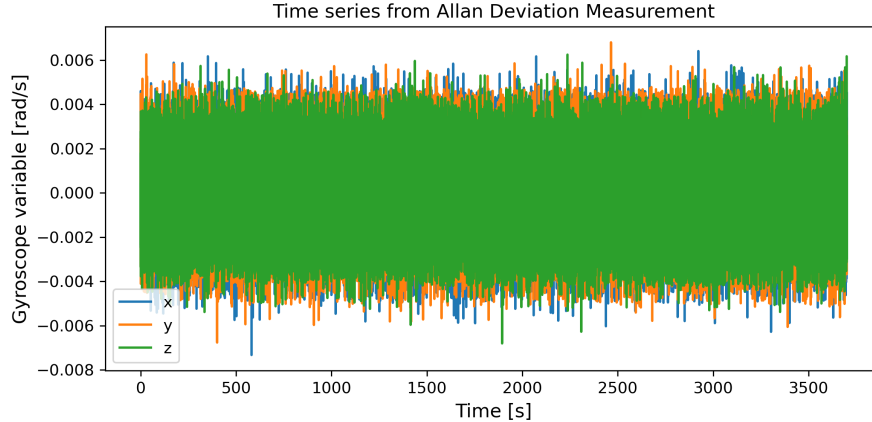


Figure 3.2.1: Time series of the Allan deviation measurement for each gyroscopic component.

the phone, which would account for the bias in the x direction. We observed the same phenomena when measuring for the rotation rate of the Earth, indicating a clear bias in the x direction.

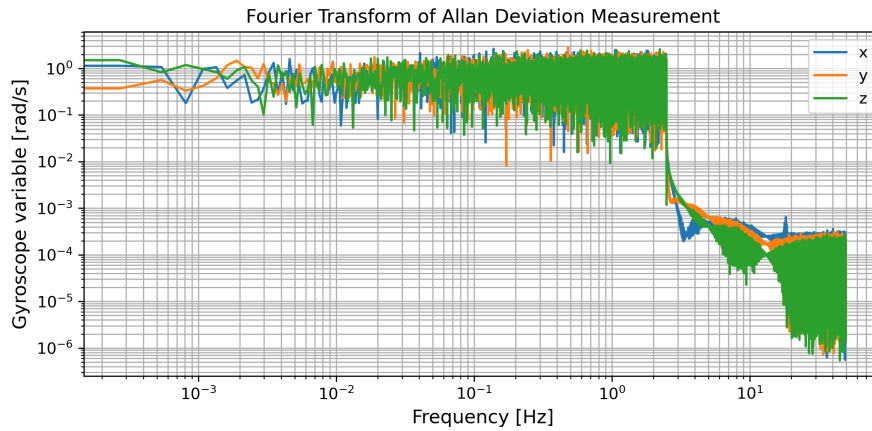


Figure 3.2.2: The Fourier spectrum of the Allan deviation measurement in each gyroscopic direction.

To determine the Allan deviation, we used the function `oadev` from the Python package `allantools` that computes the overlapping Allan deviation given the frequency data, the sample rate, and the time series of the measurement. This returns the Allan deviation for each integration time  $\tau$ . By using `oadev` instead of the standard `adev`, the noise that is apparent after the point of instability is reduced, yielding a smooth curve at each integration time. The sampling rate was obtained by taking the inverse of the timestep in the measurement, yielding a sampling rate of 99.2 Hz. Fig. 3.2.3 shows the Allan deviation for each gyroscopic component at each integration time, displayed in a log-log format.

The shot-noise time interval, which is the integration time up until the point where the instability of the instrument or drift dominates, can be determined as the point where the first minima of the plot is observed. From Fig. 3.2.3, we observe that the point of instability of the x direction occurs at a much earlier integration time than compared to those from the y and z directions. This indicates that the bias from the x direction affected the Allan deviation measurement.

We also determine the shot-noise limited sensitivity  $\mathcal{A}$  by performing a log-linear fit according to Eq. 3.2.2. By taking the logarithm on both sides, we obtain an equation that can be linearized as such:

$$\log(\sigma_{\text{ad}}) = m \log(\tau) + \log \mathcal{A} \quad (3.2.1)$$

where  $m$  should yield  $-0.5$  due to the shot-noise scaling. The shot-noise limited sensitivity can then be obtained by taking the exponential of the intercept from the log-linear fit. The data was truncated after the point of instability for each direction. Fig. 3.2.3 shows the log-linear fit for each component. Table 3.1 show the shot-noise limited time interval and the fit parameters (the slope  $m$  and the shot-noise limited sensitivity  $\mathcal{A}$ ) for each component.

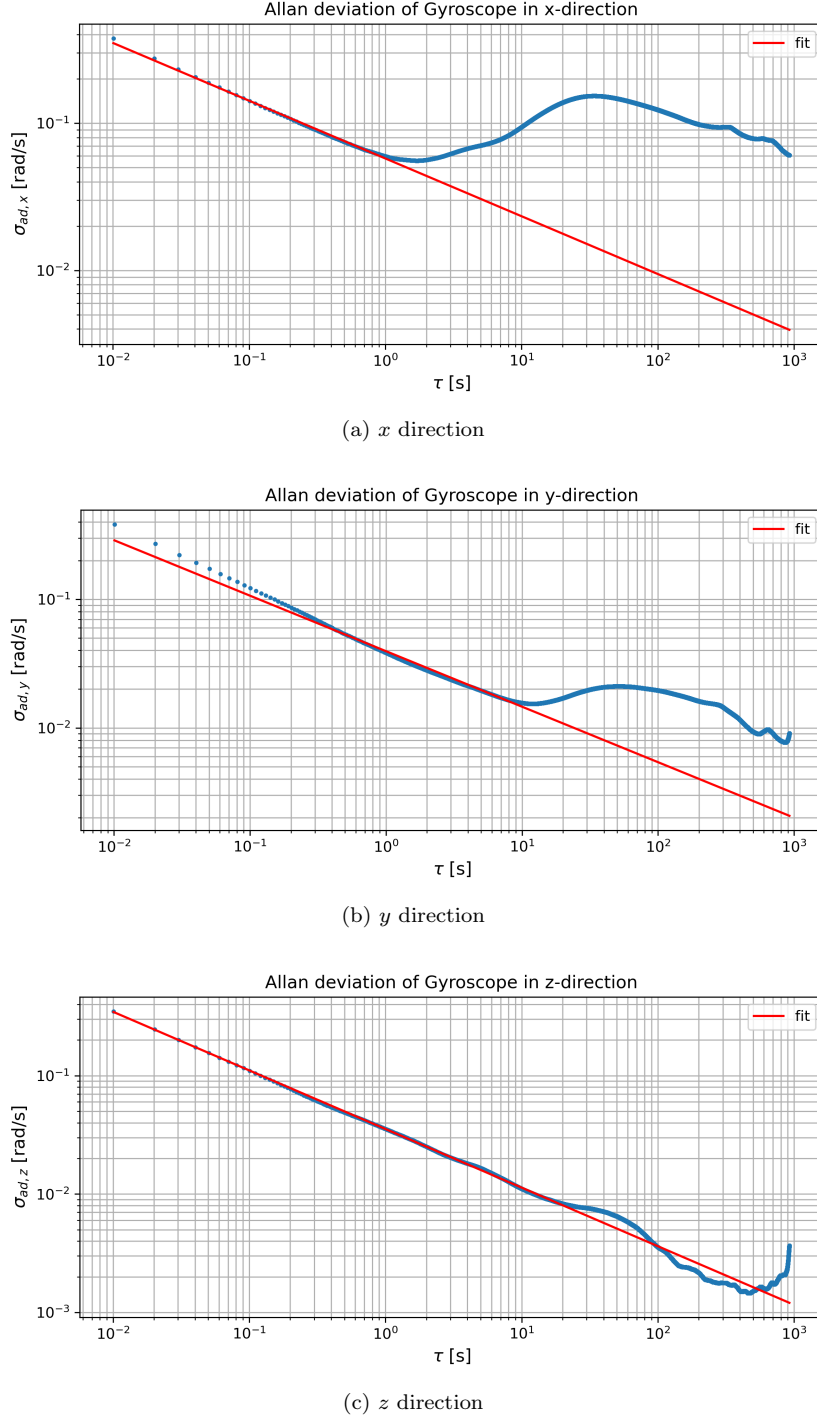


Figure 3.2.3: The Allan deviation for each gyroscopic component for each integration time  $\tau$ . The log-linear fit is also shown.

Component	$\tau$ [s]	$m$	$\mathcal{A}$ [rad/s/ $\sqrt{\text{Hz}}$ ]	$ m - (-0.5) $
x	1	-0.3925	0.0576	0.1106
y	10	-0.4318	0.0395	0.0677
z	20	-0.4952	0.0354	0.0048

Table 3.1: The shot-noise limited time interval and associated fit parameters from the log-linear fit of the Allan deviation in each component. [Fix table width](#)

We observe that the time intervals vary between each component, however  $\tau_x$  is one order of magnitude smaller than those from the y and z direction. This indicates that the bias observed in Fig. 3.2.2 influenced the measurement of the Allan deviation.

When comparing the fit parameters, we observe that the slope from the z component yield the value most closest to  $-0.5$ , which may be due to the longer shot-noise time interval, which in turn allows more data points to be fit. However, all components yield slopes close to  $-0.5$ , with the largest deviation from the x-direction with a residual of  $\sim 0.11$ . We also observe that the shot-noise limited sensitivity from the x component is approximately 0.02 larger than that of the y and z components. This again indicates the influence of the bias of measurement in the x direction. This also shows that the phone's gyroscope is more sensitive to measurements in the y and z direction as compared to that of the x direction.

### 3.3 Task 3: Rotation Rate of Earth

To determine the rotation rate of the Earth, we utilize the same method as we have performed to measure the Allan deviation, but we perform this for the shot-time limited interval derived by the section above.

We first measure the gyroscope  $x, y, z$  coordinates for the duration of the shot-time interval of  $\tau = 700\text{s}$ . After the data was recorded, we performed the same measurement but with the phone flipped upside down. This corresponds to a flip in the  $y$  direction. We then performed the same process but flipping in the  $z$ -direction instead (i.e. rotations parallel to the surface). This was performed for a shorter duration of  $\tau = 300\text{s}$  due to time constraints. The corresponding time series for both results are shown in Fig. 3.3.1, 3.3.2, 3.3.3 and 3.3.4.

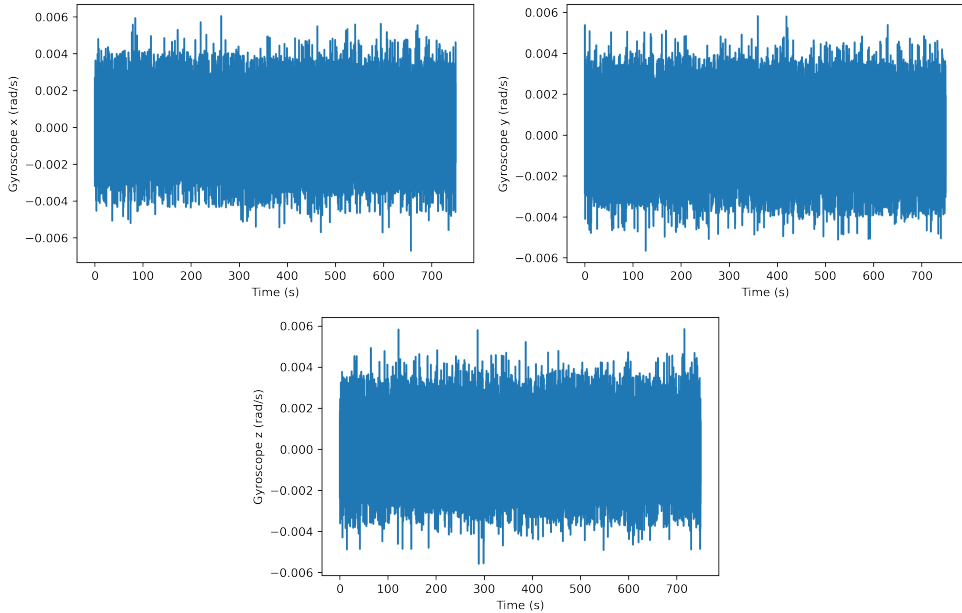


Figure 3.3.1: Raw data of all the three axes of gyroscope from phone for measurement of the Earth's rotation. The measurement was took with the phone face up.

After performing the FFT onto the resulting time series, we observed the sharp peak in the gyroscope  $x$ -direction. This shows that there is a clear bias in the  $x$ -direction of the phone gyroscope.

The temporal average of each measurement (both flipped and unflipped) was taken, and the difference between the unflipped and flipped measurements were taken (normalized by 2). For example, for the  $x$  coordinate we have:

$$\delta\bar{\omega}_x = \frac{|\bar{x}_{\text{noflip}} - \bar{x}_{\text{flip}}|}{2} \quad (3.3.1)$$

Such measurements for both rotations are tabulated on Table 3.2. The magnitude of the values are also evaluated. Note that for arbitrarily small differences, the deviations may be small and thus to properly normalize this, one needs to take into account the uncertainty in the measurement as well.

Furthermore, to properly account for the Earth's rotation rate, we need to transform from the local frame in which we observe the phone's orientation in. This can be done by a simple coordinate

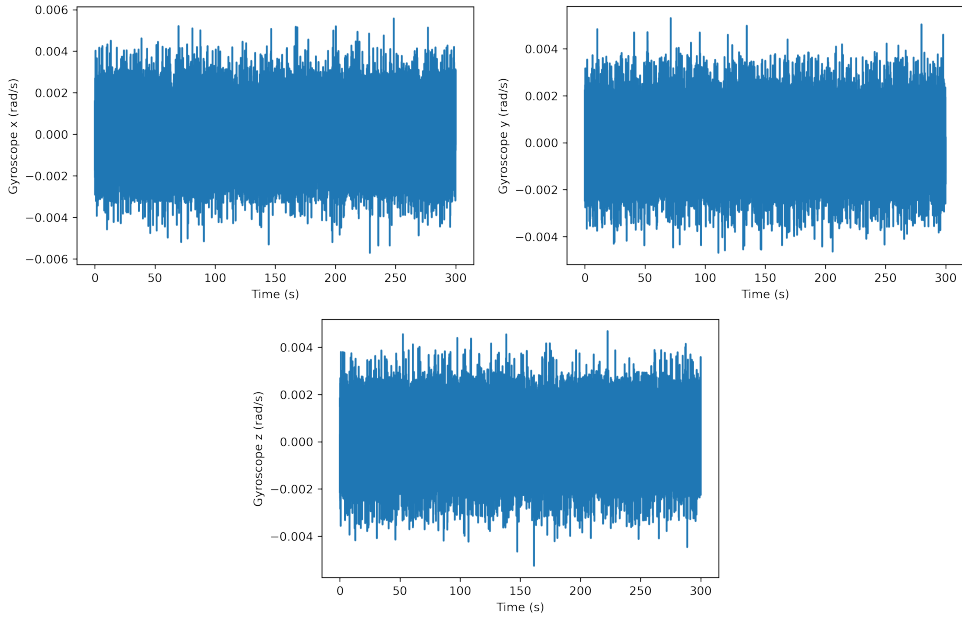


Figure 3.3.2: Same as Fig. 3.3.1 but for phone face down instead.

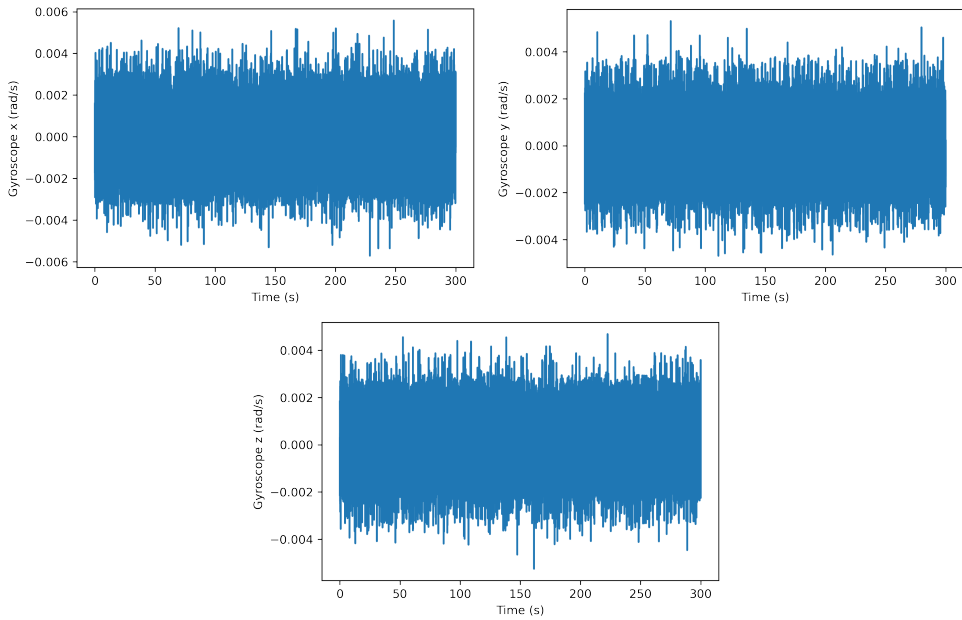


Figure 3.3.3: Same as Fig. 3.3.1 but for rotations in the  $z$ -direction. This was performed with the phone facing towards the South Pole.

transformation as such:  $\omega = \Omega_E \cos \phi$ , where  $\phi$  is the geographic latitude. With  $\phi = 39.257^\circ$  (defined from the North Pole), we obtain our corrected rotation rate of the Earth as  $\Omega_E = 3.083\mu\text{rads}^{-1}$  and  $\Omega_E = 38.80\mu\text{rads}^{-1}$  for the up/down and North/South flip case respectively.

When comparing the values of the rotation rate to the analytical value  $\Omega_{E,thr} = 72.92\mu\text{rads}^{-1}$ , both yielded values are underestimated. However, the rate where the phone was flipped upside down yielded lower values compared to that when we flipped the phone from South to North. This indicates a clear bias in the rotation and how it impacts the measurement, which is clear due to the East-West rotation of the Earth.

Furthermore, the underestimation of the values are clear due to the various systematical uncertainties that need to be accounted for. The movement of nearby people, the wind, the temperature differences can all impact the phone gyroscope in some way. The MEMS gyroscope does not have as many tools that will calibrate for such deviations as compared to our experimental setup.

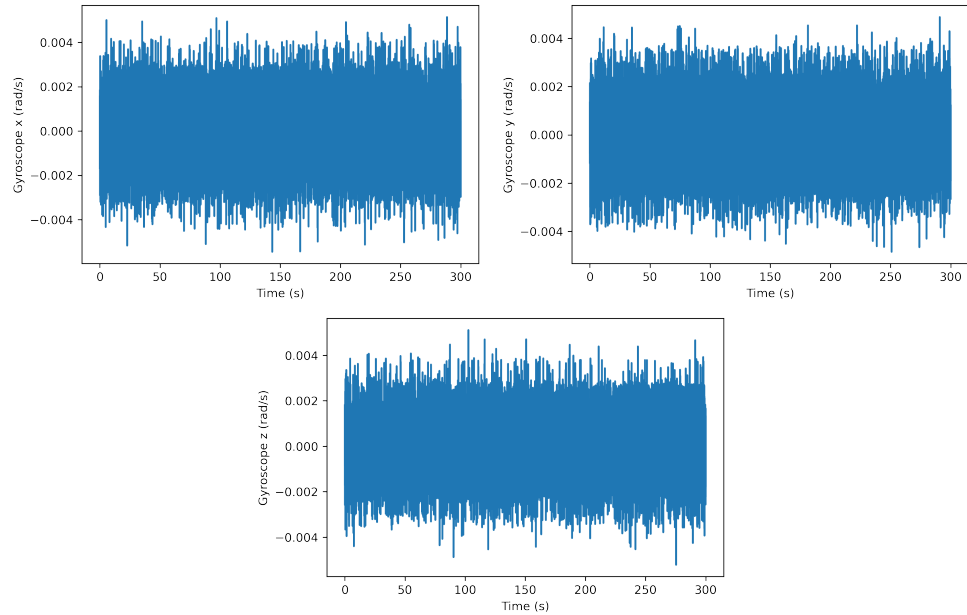


Figure 3.3.4: Same as Fig. 3.3.3 but for those facing towards the North Pole instead.

Coordinate	$\delta\bar{\omega}_i$ , face up/down (rad/s)	$\delta\bar{\omega}_i$ , face North/South (rad/s)
$x$	$9.273 \times 10^{-8}$	$9.956 \times 10^{-6}$
$y$	$4.603 \times 10^{-7}$	$2.814 \times 10^{-5}$
$z$	$2.340 \times 10^{-6}$	$3.357 \times 10^{-6}$
$\omega$	$2.386 \times 10^{-6}$	$3.004 \times 10^{-5}$

Table 3.2: Difference of temporal average of rotation rate for each gyroscopic coordinate and its magnitude.

# Chapter 4

# Experimental Set-Up and Procedure

## 4.1 Experimental Set-Up

## 4.2 Procedure

### 4.2.1 Free Spectral Range

We first measured both the signal of the laser input and after the laser has passed through the ring cavity system. The window was adjusted until three resonance peaks and their corresponding sidebands were observed. See Fig. 4.2.1 the observed raw signal.

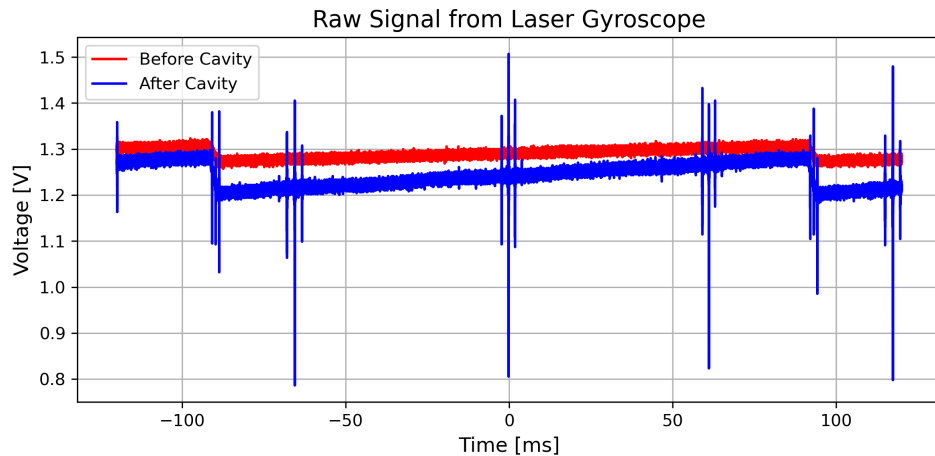


Figure 4.2.1: Raw signal input from the laser before and after passing through the ring cavity system.

As the raw data was provided in the time domain, we converted the time axis into a frequency axis. In order to do so, we use the fact that the modulation frequency from the EOM was  $\Omega = 10 \text{ MHz}$ , and we determined the width in time between the peaks and the sidebands to obtain a conversion time between the two axes. The error of the conversion time was obtained purely statistically by using the standard error of the mean.

From this conversion time, we obtained the free spectral range as the peak-to-peak difference between the resonance peaks. The error in the free spectral range was considered by observing the approximate full-width half-maximum of each peak. We then took the weighted average of the free spectral ranges to obtain an averaged free spectral range.

We then evaluated the cavity perimeter from Eq. 2.2.2 for each free spectral range that we have observed. We compared our obtained results with the measured value of the cavity perimeter  $P_{\text{meas}} = 0.990 \pm 0.005 \text{ m}$  obtained from Ref. [1].

### 4.2.2 PDH Error Signal and PID Optimization

To observe the error signal generated from PDH locking, we observed the combined signal generated from the fast and slow PID controller. Fig. 4.2.2 shows the raw signal obtained from the PDH error.

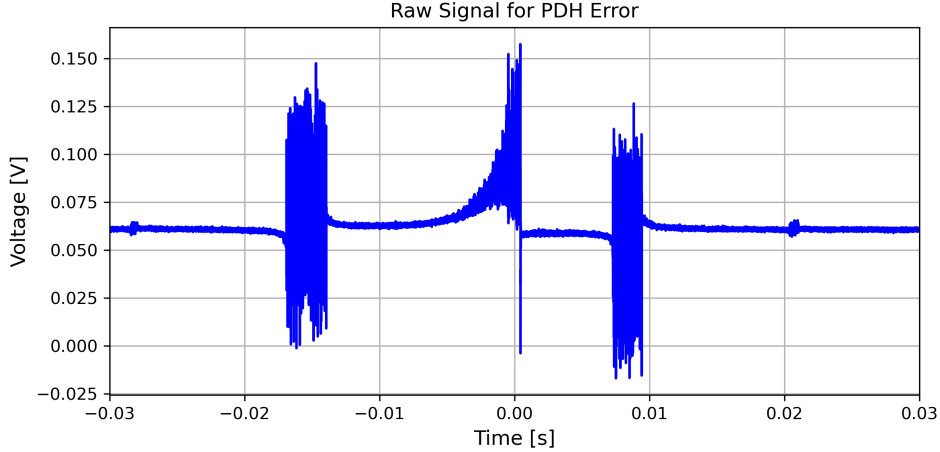


Figure 4.2.2: Raw Signal from PDH locking using the fast and slow PID controller.

The corresponding data was then used to determine the linear fit of the error signal where the zero crossing and linear slope is present (i.e. near the middle of the observed error signal). This was performed by first filtering the data using `scipy.signal.sosfilt`, then using a least-squares fit with `numpy.polyfit`. Fig. 4.2.3 shows the filtered data from the error signal generated by PDH locking. We observe that the shape of the signal closely resembles that of Fig. 2.2.2 as desired.

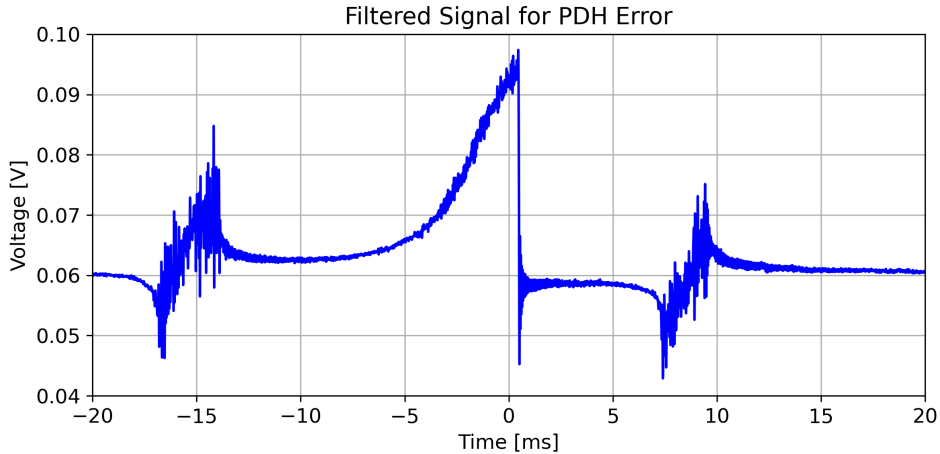


Figure 4.2.3: Filtered signal from PDH locking. The behavior of the signal closely resembles that of the signal shown in Fig. 2.2.2.

The error signal was then used to determine the optimal PID parameters that yield the most stable and large signal. In order to do this, the following parameters were modified: SLOW INT, FAST INT, DIFF GAIN, FAST DIFF / FILTER, SLOW GAIN, FAST GAIN, GAIN LIMIT, and OFFSET. The major parameters that influenced the signal were the SLOW INT, SLOW GAIN, FAST DIFF / FILTER and FAST GAIN. Modifying the SLOW INT and FAST DIFF caused the laser to be out of lock, whereas FAST GAIN decreased the noise observed in the signal. As we decreased the SLOW GAIN, we observed that the laser became more out of lock, allowing for the control of the laser locking. The OFFSET parameter adjusted the offset between the two signals. Table 4.1 shows the optimal PID parameters used in the subsequent measurements which were both stable and yielded a strong signal strength.

When performing laser locking, we further needed to consider the systematics due to the environment. Any small disturbance such as clapping, tapping the desk, moving the cables or even walking influenced

PID Parameter	Value
SLOW INT	25
FAST INT	20K
FAST DIFF / FILTER	10M
FAST GAIN	6 dB
GAIN LIMIT	30

Table 4.1: The optimal PID parameters used for this experiment. The SLOW GAIN and FAST GAIN parameter values are not noted as specific values are not marked on the Moglabs PID controller.

the degree of locking for the laser. Other factors such as the temperature fluctuations in the room may have caused the laser to be out of lock as well. In order to verify that we were obtained the correct resonant mode when optimizing the PID parameters (i.e. the  $\text{TEM}_{010}$  mode), we used a camera located on the rotation table. An image of the resulting mode obtained when locking can be seen in Fig. 4.2.4.

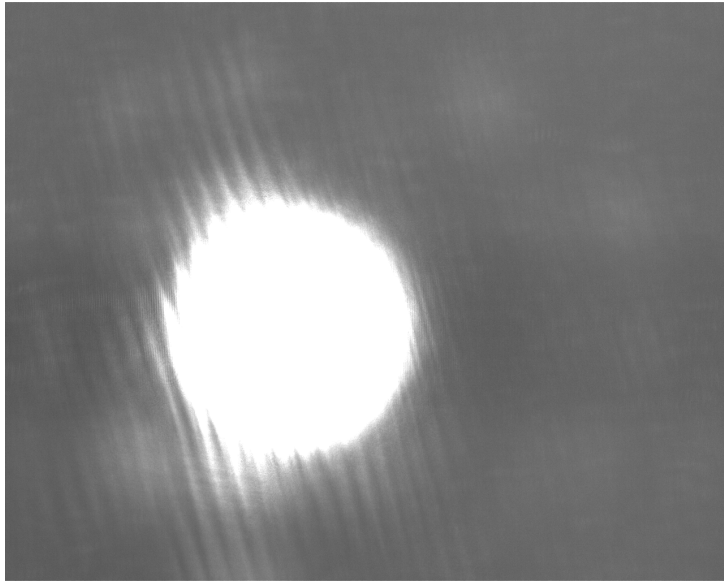


Figure 4.2.4: The Fundamental  $\text{TEM}_{0,0}$  Gaussian mode.

### 4.2.3 Cavity Ring-Down

As discussed in the 2.2.3, here we measure the exponential decay of power within the cavity after the “switch” is turned off. After setting the photodiode channel to the appropriate height, trigger mode was set to single. The laser beam is then switched off using the front panel control of the AOM driver. We notice an exponential decay, as seen in Fig. 4.2.5. Several measurements were taken out which ten were analyzed. Rest of the figures can be found in the Appendix 8. The data was analysed in Python and curve fitting was done using the following function

$$f(t) = a \exp\left(-\frac{t}{t_{dec}}\right) + c, \quad (4.2.1)$$

where  $a$  is the amplitude,  $t_{dec}$  is the decay constant and  $c$  is a constant. The fitting was done using the function `scipy.optimize.curve-fit`. The following results were obtained:

#### Locking

### 4.2.4 Scale Factor

The gyroscope table was set into rotation, all the while making sure that the cavity was still locked. The oscilloscope channel was used to read the frequency. In order to get the frequency in Hz, the encoder

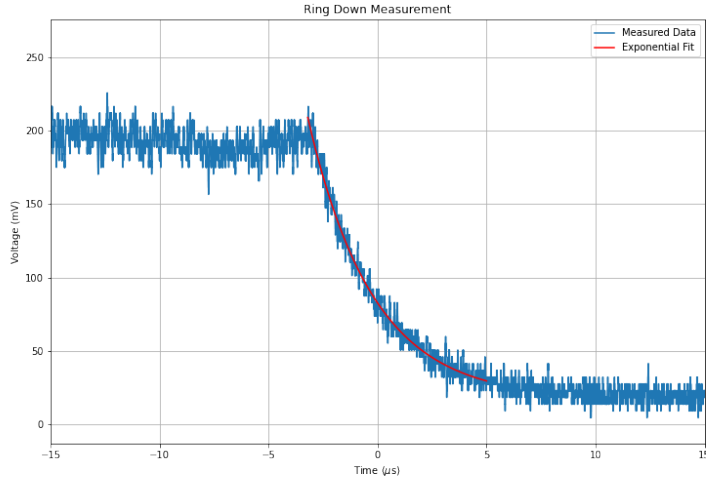


Figure 4.2.5: Exponential decay of power in the cavity after switching it off.

rate of 10,000 needs to be taken into account. Since one complete rotation corresponds to 10,000 counts, the recorded values need to be divided by 10,000 over the duration.

The beat signal was recorded from another channel and evaluated for five different voltages, which correspond to five different rotation rates. Higher rotation rates lead to highly unstable cavity, with stability of the lock not lasting more than 2-3s. Hence, lower rotation rates were preferred for a much more reliable data. Nevertheless, even at low rotation rates, the cavity falls out of lock and we had to re-lock it and continue taking readings. Another interesting thing to note is that this lock could be broken with slight disturbances like banging the table or moving the chair.

As an example, the unfiltered data for beat frequency at 1.5V is shown in Fig. ???. In order to extract usable data from this, first loose upper and lower bounds were set to make sure that unreasonably high and low values do not contribute. From `scipy.signal`, the package `savgol-filter` was used to filter the data. The filtered data is shown in Fig. ???.

**Do you know why there is a weird 0.5 next to these figures?**

Taking the average of the entire data gives us the corresponding sagnac frequency. Blah blah blah.

The scale factor is shown in Fig. 4.2.6.

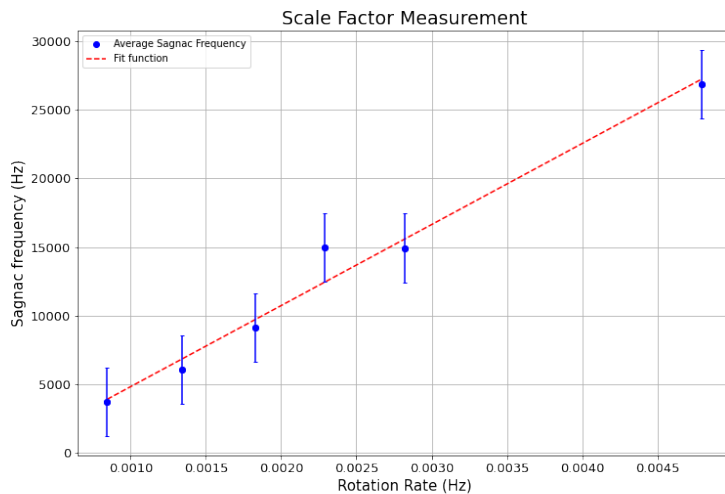


Figure 4.2.6: The sagnac frequency and their linear fit, which gives the scale factor.

#### 4.2.5 Allan Deviation

Finally, we measured the Allan deviation of the laser gyroscope. We performed the same procedure as with the scale factor measurement. Using the same PID parameters as before, we set the rotation frequency to rotate with 0.75 V, so that the laser will remain locked as long as possible. The gyroscope was rotated until the cable connecting the gyroscope did not extend or contract any further, then the same analysis was performed in the opposite rotation direction. The measurement was taken continuously for approximately 1.5 hours. The unprocessed time series for the frequency measurement can be seen in Fig. 4.2.7.

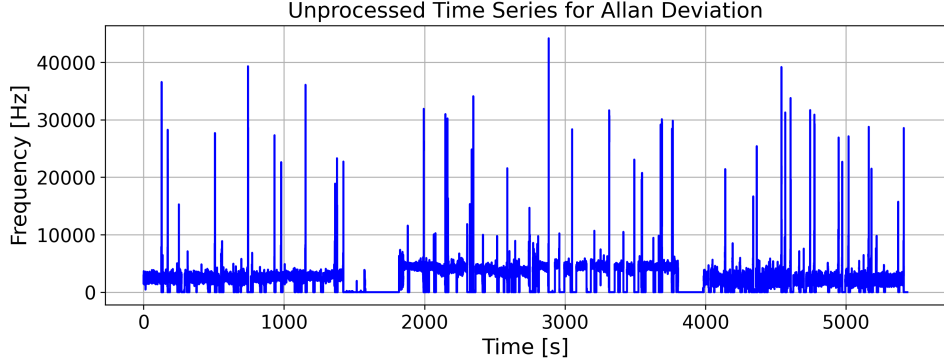


Figure 4.2.7: Unprocessed time series obtained from Allan deviation measurements. We observe large spikes at numerous locations as well as regions with zero frequency.

From the raw data, we first removed any measurements that were taken while the laser was unlocked and when the rotation of the table was switched. We then apply filtering towards our data using `scipy.signal.sosfilt` to remove fluctuations of the signal. Fig. 4.2.8 shows the measured data after filtering.

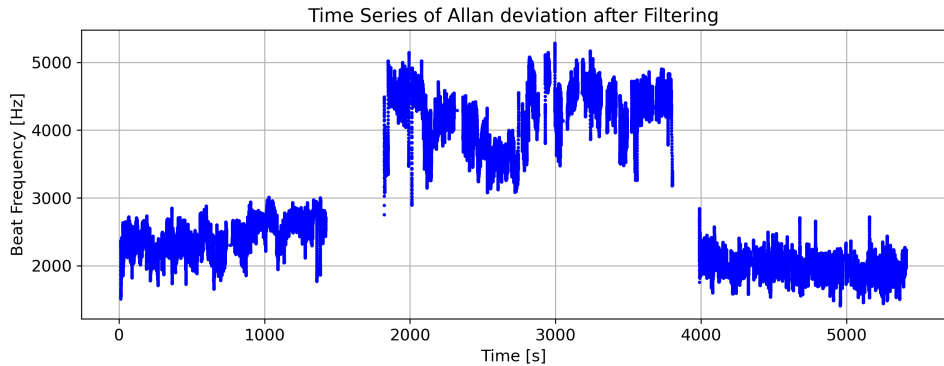


Figure 4.2.8: Time series of Allan deviation measurement after filtering and removing unwanted data measurements.

We then performed the same procedure as with the Pre-lab tasks in Sec. 3.2 to determine the Allan deviation. , namely to first determine the frequency spectrum of the signal using `scipy.fft` before passing through the frequency data into `allantools.oadev` to obtain the Allan deviation for each integration time  $\tau$ . We also determined the shot-noise limited time  $\tau$  by observing the time duration in which the instability of the measurement starts. For the rotation frequency of the table, we followed the same procedure from Sec. 4.2.4.

# Chapter 5

## Results and Discussion

### 5.1 Free Spectral Range

Table 5.1 shows the corresponding conversion time obtained from each sideband using the modulation frequency of 10 MHz. The mean conversion time that we obtained was  $2.104 \pm 0.066$  ms which is the conversion time that we used to determine the free spectral range. Fig. 5.1.1 shows the corresponding resonant peaks in both the time and frequency axis.

Sideband	Conversion time [ms]
1	2.385
2	2.226
3	2.110
4	2.003
5	1.998
6	1.900
<b>Mean</b>	$2.104 \pm 0.066$

Table 5.1: The conversion time determined from each sideband with the three resonant peaks obtained from Fig. 4.2.1. [Fix table width](#)

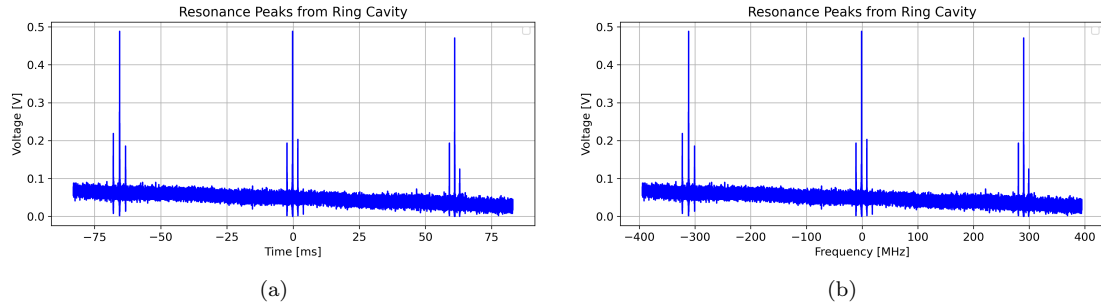


Figure 5.1.1: The observed resonant peaks from the ring cavity in the laser gyroscope. (a) and (b) show the same plot in the time and frequency domain respectively.

From the obtained conversion time, we obtained two values of the free spectral range from the peak-to-peak difference between each resonance peak. Correspondingly we also obtained two values for the cavity perimeter. Table 5.2 shows the obtained free spectral range and cavity perimeter for each peak-to-peak difference as well as their weighted average.

When comparing the average cavity perimeter to the measured values given in Ref. [1], we observed that the experimental value were  $1.52\sigma$  away. This indicates that the result we have obtained is in good, but not great agreement with the measured value. Such results may be caused by

Peak	$\delta\nu_{\text{FSR}}$ [MHz]	Cavity Perimeter [cm]
1-2	$310.60 \pm 0.12$	$96.587 \pm 0.039$
2-3	$291.12 \pm 0.11$	$103.050 \pm 0.040$
<b>Mean</b>	$299.778 \pm 0.083$	$99.760 \pm 0.028$

Table 5.2: The free spectral range  $\delta\nu_{\text{FSR}}$  and the cavity perimeter  $P$  obtained for each peak-to-peak. The weighted average is also shown. [Fix table width](#)

## 5.2 PDH Error Signal

Once applying the linear fit within the region of interest, we obtain the following parameters:  $a = -1168 \pm 580 \text{ J s}^{-2}$ ,  $b = 639.82 \pm 0.13 \text{ m J s}^{-1}$  for a linear fit of  $\epsilon_{\text{fit}} = at + b$ . The filtered data within the region of interest with the linear fit is shown on Fig. 5.2.1. As we can see, the slope is not truly vertical, indicating that there is some broadening of the cavity linewidth, as  $a \sim \sqrt{P_c P_s} \delta\nu_{\frac{1}{2}}$ . This is to be expected as thermal fluctuations as well as other disturbances can cause such broadening of the spectrum.

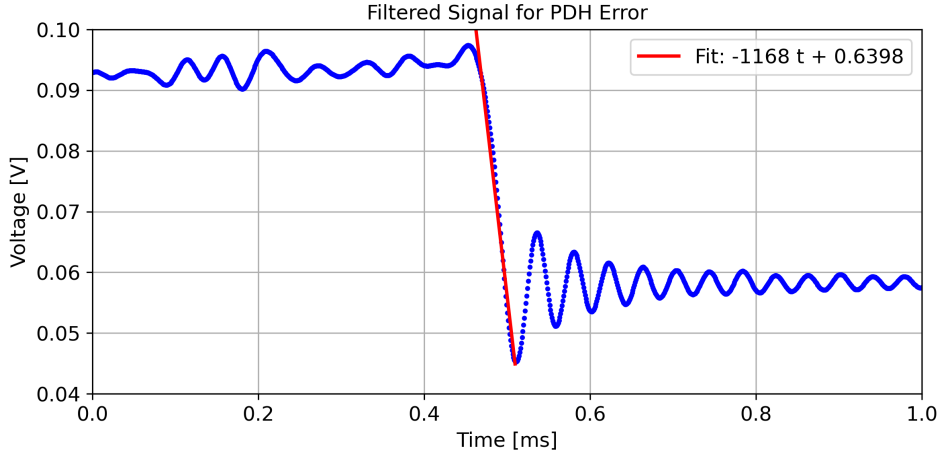


Figure 5.2.1: The filtered signal from PDH locking in a zoomed-in region. The linear fit with associated fit parameters are also shown.

As we can observe from Fig. 4.2.3, the signal cannot truly exhibit the sharp peaks as observed in the Fig. 2.2.2. Such behavior is caused by the noise of the signal generated by the surrounding environment, as well as the oscillatory behavior of the signal, which causes the zero values to be oscillatory. Thus true peaks cannot be observed which prevents us from applying a true linear fit to the data.

## 5.3 Cavity Ring-down

## 5.4 Scale Factor

## 5.5 Allan Deviation

In Fig. , we show the frequency spectrum of the measurement obtained for the Allan deviation. We observe that the laser gyroscope is at least sensitive to rotations starting from  $\sim 5 \times 10^{-4}$ . This can be noted due to the cutoff between the noise and the actual signal.

Fig. 5.5.2 shows the Allan deviation obtained for each integration time. We observe that the shot-noise time interval is approximately  $\tau = 4 \text{ s}$ , which is extensively small compared to those in typical experiments, which can yield values as high as  $\tau \sim 10^5$  [1]. Further, when we perform the linear fit, we obtain the following values for our fit parameters:

$$m = -0.6966511 \pm 0.0000016 \quad \mathcal{A} = 51163.064 \pm 0.094. \quad (5.5.1)$$

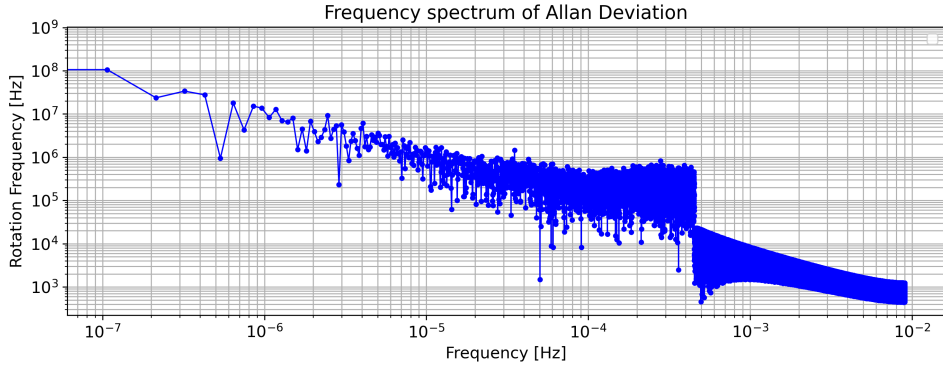


Figure 5.5.1: The frequency spectrum of the Allan deviation measurement.

When comparing with the expected power of  $-0.5$ , we see that the residual gives  $0.196$ , giving a relatively large deviation. A possible cause for this may be due to the lack of errors that needed to be taken into account. As we can see from the errors in the fit parameters, the errors are largely underestimated, indicating that we have neglected to consider other errors into account. Furthermore, the gyroscope sensitivity

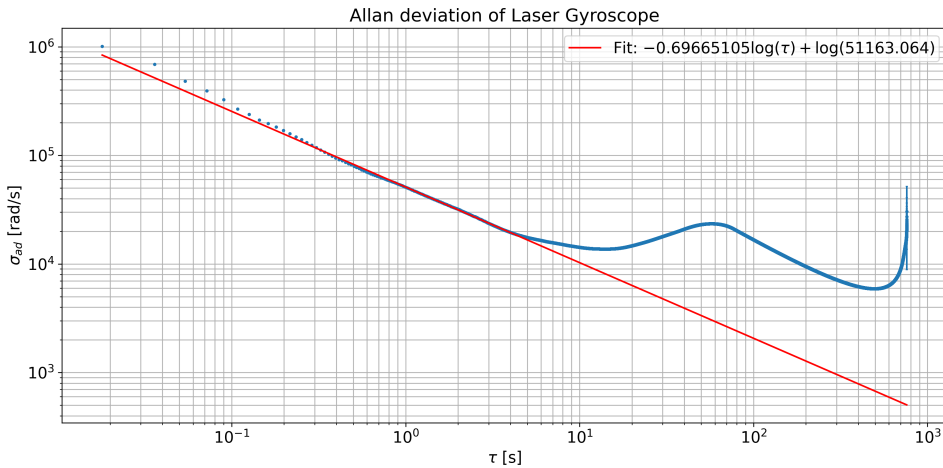


Figure 5.5.2: The Allan deviation of the laser gyroscope, plotted against the integration time in a log-log plot. The log-linear fit is also shown.

From Fig. 5.5.2, This is a much lower duration compared to typical gyroscope measurements, which can yield integration times

## 5.6 Rotation Rate of the Earth

## **Chapter 6**

# **Conclusion and Outlook**

## Chapter 7

# Acknowledgements

# Bibliography

- [1] T. Groh and S. Stellmer, “Laser gyroscope: A249 - course description,” Aug. 2021.
- [2] D. Behrend, C. Thomas, J. Gipson, E. Himwich, and K. Le Bail, “On the organization of cont17,” *Journal of Geodesy*, vol. 94, no. 10, p. 100, Oct. 2020, ISSN: 1432-1394. DOI: [10.1007/s00190-020-01436-x](https://doi.org/10.1007/s00190-020-01436-x).
- [3] F. Wettzell. “Large laser gyroscopes for monitoring earth rotation.” (Nov. 2005), [Online]. Available: <http://www.fs.wettzell.de/LKREISEL/G/LaserGyros.html> (visited on 04/30/2022).
- [4] N. Beverini, A. D. Virgilio, J. Belfi, *et al.*, “High-accuracy ring laser gyroscopes: Earth rotation rate and relativistic effects,” *Journal of Physics: Conference Series*, vol. 723, p. 012061, Jun. 2016. DOI: [10.1088/1742-6596/723/1/012061](https://doi.org/10.1088/1742-6596/723/1/012061).
- [5] O. Darrigol, “Georges sagnac: A life for optics,” *Comptes Rendus Physique*, vol. 15, no. 10, pp. 789–840, 2014, The Sagnac effect: 100 years later / L’effet Sagnac : 100 ans après, ISSN: 1631-0705. DOI: <https://doi.org/10.1016/j.crhy.2014.09.007>.
- [6] M. von Laue, “About an experiment on the optics of moving bodies,” *Munich session reports 1911*, pp. 405–412, 1911.
- [7] E. Benedetto, F. Feleppa, I. Licata, H. Moradpour, and C. Corda, “On the general relativistic framework of the sagnac effect,” *The European Physical Journal C*, vol. 79, no. 3, p. 187, Mar. 2019, ISSN: 1434-6052. DOI: [10.1140/epjc/s10052-019-6692-9](https://doi.org/10.1140/epjc/s10052-019-6692-9).
- [8] Z. Feng, Y. He, W. Yan, F. Yang, W. Han, and Z. Li, “Progress of waveguide ring resonators used in micro-optical gyroscopes,” *Photonics*, vol. 7, no. 4, 2020, ISSN: 2304-6732. DOI: [10.3390/photonics7040096](https://doi.org/10.3390/photonics7040096).
- [9] I. Kudelin, S. Sugavanam, and M. Chernysheva, “Rotation active sensors based on ultrafast fibre lasers,” *Sensors*, vol. 21, no. 10, 2021, ISSN: 1424-8220. DOI: [10.3390/s21103530](https://doi.org/10.3390/s21103530).
- [10] *Pound-drever-hall locking with the fsc*, AN002, Moglabs.
- [11] K. Liu, F. L. Zhang, Z. Y. Li, *et al.*, “Large-scale passive laser gyroscope for earth rotation sensing,” *Opt. Lett.*, vol. 44, no. 11, pp. 2732–2735, Jun. 2019. DOI: [10.1364/OL.44.002732](https://doi.org/10.1364/OL.44.002732).

# Chapter 8

## Appendix

# Bibliography

- [1] T. Groh and S. Stellmer, “Laser gyroscope: A249 - course description,” Aug. 2021.
- [2] D. Behrend, C. Thomas, J. Gipson, E. Himwich, and K. Le Bail, “On the organization of cont17,” *Journal of Geodesy*, vol. 94, no. 10, p. 100, Oct. 2020, ISSN: 1432-1394. DOI: [10.1007/s00190-020-01436-x](https://doi.org/10.1007/s00190-020-01436-x).
- [3] F. Wettzell. “Large laser gyroscopes for monitoring earth rotation.” (Nov. 2005), [Online]. Available: <http://www.fs.wettzell.de/LKREISEL/G/LaserGyros.html> (visited on 04/30/2022).
- [4] N. Beverini, A. D. Virgilio, J. Belfi, *et al.*, “High-accuracy ring laser gyroscopes: Earth rotation rate and relativistic effects,” *Journal of Physics: Conference Series*, vol. 723, p. 012061, Jun. 2016. DOI: [10.1088/1742-6596/723/1/012061](https://doi.org/10.1088/1742-6596/723/1/012061).
- [5] O. Darrigol, “Georges sagnac: A life for optics,” *Comptes Rendus Physique*, vol. 15, no. 10, pp. 789–840, 2014, The Sagnac effect: 100 years later / L’effet Sagnac : 100 ans après, ISSN: 1631-0705. DOI: <https://doi.org/10.1016/j.crhy.2014.09.007>.
- [6] M. von Laue, “About an experiment on the optics of moving bodies,” *Munich session reports 1911*, pp. 405–412, 1911.
- [7] E. Benedetto, F. Feleppa, I. Licata, H. Moradpour, and C. Corda, “On the general relativistic framework of the sagnac effect,” *The European Physical Journal C*, vol. 79, no. 3, p. 187, Mar. 2019, ISSN: 1434-6052. DOI: [10.1140/epjc/s10052-019-6692-9](https://doi.org/10.1140/epjc/s10052-019-6692-9).
- [8] Z. Feng, Y. He, W. Yan, F. Yang, W. Han, and Z. Li, “Progress of waveguide ring resonators used in micro-optical gyroscopes,” *Photonics*, vol. 7, no. 4, 2020, ISSN: 2304-6732. DOI: [10.3390/photonics7040096](https://doi.org/10.3390/photonics7040096).
- [9] I. Kudelin, S. Sugavanam, and M. Chernysheva, “Rotation active sensors based on ultrafast fibre lasers,” *Sensors*, vol. 21, no. 10, 2021, ISSN: 1424-8220. DOI: [10.3390/s21103530](https://doi.org/10.3390/s21103530).
- [10] *Pound-drever-hall locking with the fsc*, AN002, Moglabs.
- [11] K. Liu, F. L. Zhang, Z. Y. Li, *et al.*, “Large-scale passive laser gyroscope for earth rotation sensing,” *Opt. Lett.*, vol. 44, no. 11, pp. 2732–2735, Jun. 2019. DOI: [10.1364/OL.44.002732](https://doi.org/10.1364/OL.44.002732).